9-18-2008

Investigating Tropical Cyclone-Climate Feedbacks Using the TRMM Microwave Imager and the Quick Scatterometer

Ryan L. Sriver
Purdue University

Matthew Huber
Purdue University, mhuber@purdue.edu

Jesse Nusbaumer
Purdue University

Geochemistry Geophysics Geosystems G3
AN ELECTRONIC JOURNAL OF THE EARTH SCIENCES
Published by AGU and the Geochemical Society

Article
Volume 9, Number 9
18 September 2008
Q09V11, doi:10.1029/2007GC001842
ISSN: 1525-2027

Investigating tropical cyclone-climate feedbacks using the TRMM Microwave Imager and the Quick Scatterometer

Ryan L. Sriver
Department of Earth and Atmospheric Sciences, Purdue University, West Lafayette, Indiana 47907, USA (rsriver@purdue.edu)

Matthew Huber
Department of Earth and Atmospheric Sciences, Purdue University, West Lafayette, Indiana 47907, USA

Purdue Climate Change Research Center, Purdue University, West Lafayette, Indiana 47907, USA

Jesse Nusbaumer
Department of Earth and Atmospheric Sciences, Purdue University, West Lafayette, Indiana 47907, USA

[1] Sea surface temperature (SST) and near-surface winds from the Tropical Rainfall Measuring Mission (TRMM) Microwave Imager (TMI) and the Quick Scatterometer (QuikScat) are used to calculate globally integrated tropical cyclone-induced SST anomalies and power dissipation (PD). We estimate tropical cyclone-induced upper ocean cooling to be ~35% higher than our previous estimates based on reanalyzed ERA40 and NCEP surface data. Annually averaged, global PD estimates from TMI are $\sim 5 \times 10^{19}$ J for the years 1998 to 2006 (roughly 30% greater than ERA40 PD for overlapping years). QuikScat PD is estimated to be $\sim 1.7 \times 10^{20}$ J for the years 2000 to 2006. On the basis of these results, we conclude that the cyclone-induced cooling signal appears to be underrepresented in ERA40 and NCEP reanalysis, as postulated in recent observational and modeling studies. Furthermore, we observe a strong positive relationship between PD and ocean surface cooling, providing further evidence for the likelihood of cyclone-induced climatic feedbacks. These results support the hypothesis that tropical cyclones play an active role in the tropical surface ocean heat budget by cooling the tropical upper oceans through enhanced vertical mixing, which likely represents a net warming beneath the oceanic mixed layer. Thus, to the degree that vertical mixing is important for regulating the ocean's meridional overturning circulation and poleward heat transport, tropical cyclones may be an important contributor to Earth's climate system. This further confirms the results of Emanuel (2001, 2002) and Sriver and Huber (2007b) that possible future changes in integrated cyclone intensity associated with warmer SST may provide possible climatic feedbacks through enhanced vertical mixing and increased ocean heat transport, thus buffering the tropics to increased temperatures while amplifying the warming at higher latitudes.

Components: 9569 words, 9 figures.

Keywords: tropical cyclones; climate feedbacks; ocean heat content; ocean mixing; diffusivity.

Index Terms: 1620 Global Change: Climate dynamics (0429, 3309); 1616 Global Change: Climate variability (1635, 3305, 3309, 4215, 4513); 1635 Global Change: Oceans (1616, 3305, 4215, 4513).

Received 29 October 2007; **Revised** 28 April 2008; **Accepted** 17 July 2008; **Published** 18 September 2008.

Sriver, R. L., M. Huber, and J. Nusbaumer (2008), Investigating tropical cyclone-climate feedbacks using the TRMM Microwave Imager and the Quick Scatterometer, *Geochem. Geophys. Geosyst.*, *9*, Q09V11, doi:10.1029/2007GC001842.

Theme: Interactions Between Climate and Tropical Cyclones on All Timescales
Guest Editors: K. Emanuel, Jay Gulledge, M. Huber, M. Mann, and P. J. Webster

1. Introduction

[2] The relationship between tropical cyclone (cyclone hereafter) activity and climate is well studied from the standpoint of how climate variability leads to changes in cyclone frequency and intensity. Studies span a full range of spatial and temporal scales: from interannual cycles such as the Quasi-Biennial zonal wind Oscillation [*Landsea et al.*, 1999], the North Atlantic Oscillation [*Elsner et al.*, 2000], and the El Nino Southern Oscillation [*Pielke and Landsea*, 1999], to multidecadal changes in temperature patterns associated with naturally varying processes such as the Atlantic Multidecadal Oscillation [*Goldenberg et al.*, 2001]. Other studies have attempted to assess the influence of human-induced warming on lower-frequency cyclone variability [*Mann and Emanuel*, 2006; *Santer et al.*, 2006].

[3] Currently, attempts to understand the effects of observed warming on cyclone activity using metrics such as storm counts [*Mann and Emanuel*, 2006; *Holland and Webster*, 2007], landfall rates [*Landsea*, 2007; *Holland*, 2007], per-storm intensity [*Kossin et al.*, 2007], and globally integrated intensity [*Emanuel*, 2005; *Sriver and Huber*, 2006] comprise an area of active scientific debate [*Shepherd and Knutson*, 2006; *Maue and Hart*, 2007; *Sriver and Huber*, 2007a, 2007b; *Emanuel et al.*, 2008]. While attempts to understand the effects of changing climate on cyclone activity is an active area of scientific research, the possibility of cyclone-induced climatic feedbacks is only beginning to gain attention.

[4] Tropical cyclones are efficient upper ocean mixers [*Jacob et al.*, 2000; *D'Asaro*, 2003]. This mixing results primarily from near-inertial wave breaking which causes cold water entrainment at the base of the mixed layer [*Shay et al.*, 1998]. This mixing is evidenced by the depressed surface temperatures observed along storm wakes [*Price*, 1981] and is accompanied by positive heat anomalies below the oceanic mixed layer [*Zedler et al.*, 2002].

[5] A recent hypothesis proposed that cyclone-induced mixing may significantly contribute to sustaining the oceans' meridional overturning circulation [*Emanuel*, 2001], a large-scale circulation pattern intimately linked to poleward ocean heat transport [*Wunsch and Ferrari*, 2004]. The strength of the meridional overturning circulation and the magnitude of poleward ocean heat transport are both sensitive to vertical ocean mixing in the tropics [*Scott and Marotzke*, 2002; *Bugnion et al.*, 2006], and recent model results suggest the mechanical energy input to the ocean by tropical cyclones may be important for regulating the oceanic general circulation [*Liu et al.*, 2008]. Furthermore, *Emanuel* [2002] suggested a strong dependence of cyclone activity on climate, and recent studies have supported this hypothesis with observational evidence that low-frequency cyclone variability is well correlated with changes in tropical surface temperature [*Emanuel*, 2005; *Webster et al.*, 2005; *Sriver and Huber*, 2006].

[6] *Sriver and Huber* [2007b, hereinafter referred to as SH07] attempted to illuminate the existence of cyclone-induced climatic feedbacks through the use of reanalysis data. SH07 utilized near-surface temperature records from ERA40 [*Uppala et al.*, 2005] and NCEP to measure cyclone-induced surface temperature anomalies, which were used to estimate downward oceanic heat pumping associated with cyclone-induced vertical mixing. On timescales long enough to assume steady state vertically integrated tropical temperatures, positive heat anomalies induced by tropical cyclone pumping must be advected out of storm-affected regions as ocean heat transport [*Emanuel*, 2001]. Results of SH07 supported *Emanuel*'s [2001] hypothesis but suggested that only ~15% of peak ocean heat transport may be associated with cyclone-induced vertical ocean mixing. Furthermore, these estimates of anomalous ocean heat content (OHC) were shown to be highly correlated with surface temperature, and a positive relationship was observed between cyclone-induced OHC anomalies and integrated cyclone intensity, thus supporting the

proposed [*Emanuel*, 2002] conditions for the existence of cyclone-induced feedbacks through vertical mixing, heat transport, and ocean temperature.

[7] In SH07, we hypothesized that better temperature and wind data sets might increase our estimates of tropical cyclone-induced anomalous OHC and integrated cyclone intensity (power dissipation) compared to prior work. Here we utilize surface temperature and wind data from the Tropical Rainfall Measuring Mission (TRMM) Microwave Imager (TMI) and the Quick Scatterometer (QuikScat) to further examine cyclone-induced climatic feedbacks discussed in SH07. Results complement the previous study based on reanalyzed winds and temperature by using up-to-date satellite measurements at higher spatial and temporal resolutions that are derived independently of reanalysis fields. We attempt to circumvent the criticisms of Best Track winds and reanalyzed surface winds [*Manning and Hart*, 2007; *Maue and Hart*, 2007] and temperature by utilizing self-consistent, objective data sets. The time series for TMI and QuikScat are much shorter than for typical reanalysis data sets (9 years for TMI and 7 years for QuikScat); however, use of TMI offers a unique opportunity to examine wind and temperature data derived using the same instrument, and QuikScat winds have been applied extensively to tropical cyclone research. This paper is organized as follows: section 2 discusses the TMI and QuikScat instruments, section 3 details the methods used in our study, section 4 contains our essential results and discusses the relationship between cyclone-induced anomalous ocean heat content and integrated intensity, and section 5 provides a summary of our conclusions and their implications.

2. TRMM TMI and QuikScat

[8] The Tropical Rainfall Measuring Mission (TRMM) Microwave Imager (TMI) is a passive microwave radiometer with nine channels ranging from 10.7 to 85 GHz [*Wentz et al.*, 2000]. It is based upon the Special Sensor Microwave/Imager (SSM/I), with a key difference being the addition of two 10.7 GHz channels with horizontal and vertical polarizations [*Kummerow et al.*, 1998]. Available geophysical parameters derived from TMI include sea surface temperature (SST), surface wind speeds, atmospheric water vapor, liquid cloud water, and rain rates. These data are freely available from the Remote Sensing Systems through their Web site: http://www.remss.com. SST is retrieved at the low end of the frequency range (10.7 GHz), and two separate surface wind speeds are derived from the 11 GHz and 37 GHz channels.

[9] The TRMM satellite was launched in November 1997 and continues to be operational today. The satellite maintains an equatorial orbit yielding a coverage of ~40°S to 40°N, and it returns global coverage on a timescale of 2 to 3 days [*Gentemann et al.*, 2004]. TMI offers a significant improvement over traditional infrared radiometers in its ability to retrieve SST from beneath clouds, which are nearly transparent at the low end of TMI's frequency range. This feature makes TMI useful for analyzing short-term surface temperature anomalies in the tropics, where persistent cloud cover can be a factor. A drawback of the radiometer is its inability to retrieve SST and surface winds through precipitation and heavy cloudiness. TMI winds have not been validated above 20 m/s, but recent results show this data to accurately reproduce individual storm intensities when scaling techniques are applied [*Hoshino and Nakazawa*, 2007].

[10] QuikScat winds are measured using the SeaWinds microwave scatterometer on board the QuikBird satellite launched in June of 1999. This Ku-band microwave (13.4 GHz) scatterometer retrieves 10 m wind velocities with respect to surface currents within a 1800 km swath, with accurate wind retrievals confined to the innermost 1600 km of the swath [*Chelton and Freilich*, 2005]. We use the 0.25° × 0.25° globally gridded QuikScat winds available through the Remote Sensing Systems (http://www.remss.com) (Version-3). These data contain two daily maps corresponding to the ascending and descending passes, as well as 3-day averaged wind fields. Retrievals are derived using the Ku-2001 model function and exhibit agreement with observation-based winds up to 50 m/s [*Wentz et al.*, 2001]. We implement QuikScat wind speeds from 2000 to 2006 in this study for comparison with TMI-derived wind quantities.

3. Methods

3.1. Data

[11] Cyclone track data is derived from the Best Track data set, composed of track information originally from the National Hurricane Center (for the northern Atlantic and northeastern Pacific regions) and the Joint Typhoon Warning Center (for the northwestern Pacific, northern Indian, and

Southern Hemisphere regions). Minor corrections have been applied to account for duplicate tracks and wind records between basins, specifically in the northeastern and northwestern Pacific regions where basin boundaries are poorly defined. Other than these minor corrections for two or three storms, these tracks are consistent with the data used in previous studies, and we refer the reader to *Sriver and Huber* [2006, 2007a, 2007b] for a complete discussion regarding use of the Best Track data set.

[12] We employ two separate methods for combining the daily passes and 3-day averaged SST and wind fields from TMI to obtain daily maps with maximum spatial coverage. In one method, we spatially average the ascending and descending passes and fill in the remaining gaps with the 3-day averaged fields. The second method compares the daily ascending and descending passes, keeping the largest returned values at overlapping grid points. We fill in the remaining gaps with the 3-day averaged fields. Our main results are not sensitive to the choice of data blending, i.e., year-to-year variability is preserved. Thus, given that a primary focus of this work is to identify cyclone winds as opposed to the background wind field, we primarily show results for the method that returns the largest values of surface wind and SST at each location. Our assumption relies on the idea the strongest returned wind at a given location is likely to be most relevant for our study.

[13] Our blending method creates a nearly complete daily representation of surface wind speed and temperature for TMI's spatial range. Some gaps remain in the data attributable to areas with persistent rain. In order to fill these regions, we utilized a mathematical relaxation technique which solves Poisson's equation. This technique likely underrepresents the magnitudes of the winds within cyclones where wind profiles contain local maxima near the storm center; however, no further correction is applied here. The missing data may slightly impact the global values of the quantities observed, but it does not appear to impact the trends when compared to independent analyses using winds from QuikScat and Best Track. We have explored the sensitivity of our conclusions to different methodologies for infilling missing values and found our results to be robust.

[14] We primarily show results for wind records derived from TMI's 11 GHz channel, which yield higher cyclone winds than the 37 GHz channel. The difference is likely due to the transparency of nonprecipitating clouds at the low end of the TMI frequency range, but we do not attempt to explicitly identify the differences here. It is noted that trends in the normalized wind-derived time series do not change as a result of the choice between 11 and 37 GHz winds.

[15] QuikScat winds are analyzed similarly to TMI. We combine daily ascending and descending passes, keeping the largest returned wind values at overlapping indices. Remaining gaps in the gloabally gridded daily maps are filled in with the 3-day averaged wind fields. This method returns nearly complete daily maps, and we do not apply further infilling of missing data. As a quality check of QuikScat winds, we sampled wind speeds along cyclone tracks from our QuikScat daily maps and compared the highest recorded values with the corresponding Best Track maximum sustained winds. We only considered QuikScat wind samples that were retrieved from an ascending or descending pass within + or −3 h of the corresponding best track estimation. Results yielded 4145 wind value comparisons, considering all Best Track storms globally from 2000 to 2006. Performing a linear regression between the Best Track maximum sustained wind speed and the corresponding maximum QuikScat wind speed from the daily maps yielded a correlation R^2 = 0.59.

3.2. Integrated Cyclone Intensity

[16] We define integrated cyclone intensity as the power dissipation (PD) [*Emanuel*, 2005; *Sriver and Huber*, 2006, 2007a, 2007b],

$$PD = 2\pi \int \int C_D \rho_a |V|^3 r dr dt$$

where C_d is surface drag coefficient, ρ_a is surface air density, $|V|$ is magnitude of the surface wind, and the integral is over the radius (r) and lifetime (t) of the storm. For all calculations, C_D and ρ are held constant and equal to 0.002 and 1 kg/m^3, respectively. PD represents the amount of power dissipated over the lifetime of a storm by surface friction; thus it also indicates the amount of energy available for ocean mixing. Because PD is the convolution of cyclone wind speed, size, and duration, it is a useful quantity for examining annual trends in regional and global cyclone activity (when PD is integrated over the number of storms annually).

3.3. Cyclone-Induced Anomalous Ocean Heat Content

[17] Following the formalism of *Emanuel* [2001], and consistent with *Sriver and Huber* [2007b], we estimate cyclone-induced, vertically integrated anomalous ocean heat content (OHC) as:

$$OHC = \int\int\int F\rho_s C\Delta T dh dW dL$$

where

- F fraction of heat transported downward from the oceanic mixed layer;
- ρ_s density of seawater;
- C heat capacity of seawater;
- ΔT magnitude of surface temperature anomaly;
- dh depth of temperature anomaly;
- dW cross track length of storm wake;
- dL long track length of storm wake.

For all calculations, ρ and C are held constant and equal to 1020 kg/m^3 and 3900 J/(kg°C), respectively.

[18] We invoke two separate methods for considering the mixing depth (dh). First, we assume mixing depths for all surface temperature anomalies are constant and equal to 50 m. This simplified approach corresponds to our previous methodology (see SH07), and the choice is consistent with recent CBLAST results, where in situ measurements for Hurricane Frances show a turbulent mixing depth of ~50 m [*Black et al.*, 2007]. In our second method, we combine surface temperature anomalies with seasonally averaged vertical ocean temperature profiles from the World Ocean Atlas (1998) [*Levitus et al.*, 2000] to estimate the annual mixed layer depth change attributable to cyclone mixing. We use the relation $L = \Delta T\frac{\partial z}{\partial T}$ (where L is the vertical mixing depth, dT is the surface temperature anomaly, and dz/dT is the vertical temperature gradient) to estimate the depth to which mixing must occur in order to achieve the observed surface temperature anomaly. With this method, we consider only the largest surface temperature anomaly (i.e., mixing event) at each location annually to avoid accounting for subsequent events that potentially remix the same regions. In both methods, we assume the surface temperature anomaly represents homogeneous mixing throughout the entire vertical mixing depth (L).

[19] In all calculations of cyclone-induced anomalous OHC, we assume all heat lost from the near-surface depth (L) is pumped down beneath the mixed layer (F = 1 in equation (2)) and that the mixed layer temperatures are eventually restored to climatologically normal conditions through surface fluxes, leading to a column-integrated heating. Analysis shows this reheating is typically on timescales of 1 to 2 weeks. These assumptions reflect a simplified approach where we do not account for surface fluxes associated with latent heating during storm passage [*Trenberth and Fasullo*, 2007]. However, since the majority (>70%) of cyclone-induced upper ocean cooling is due to entrainment through the base of the mixed layer [*Shay et al.*, 1992; *Shay et al.*, 1998; *Jacob et al.*, 2000; *D'Asaro*, 2003], our approach offers a valid first-order approximation of vertical ocean heat pumping by these events.

3.4. Cyclone Footprint

[20] Wind speeds and temperature are analyzed every 6 h over a spatial domain that is centered on the best track location and moves with each storm (consistent with the methods of SH07). Given that our methodology creates daily maps of SST and surface winds, our technique may not be capturing variability on timescales less than a day. This limitation does not largely affect SST, since cyclone-induced anomalies are on the order of 4–7 days; however, the typical hourly evolution of cyclone winds may not be adequately represented. In this respect, data sources such as ERA40, with higher temporal resolution may be better for capturing the subdaily evolution of the cyclone wind fields. But ERA40's lower spatial resolution and poor representation of tropical cyclone structure [*Manning and Hart*, 2007] is a limitation compared to TMI or QuikScat. At this point, it is not clear how the tradeoffs between spatial and temporal limitations between various data sets and methodologies affect the different aspects of estimating storm evolutions, but the assumptions made in this study do not appear to affect our essential results. For estimating trends in integrated cyclone intensity (PD or PD index), we observe similar results using TMI, QuikScat, Best Track, and recent NCDC time series created by *Kossin et al.* [2007].

[21] We tested the sensitivity of our PD results to the choice of footprint domain size (6° × 6°, 8° × 8°, 10° × 10°), and the trends did not change. Furthermore, we applied several minimum wind thresholds (0, 10, 17 m/s) in combination with varying domain sizes to ensure the noncyclone background wind fields did not bias our PD results.

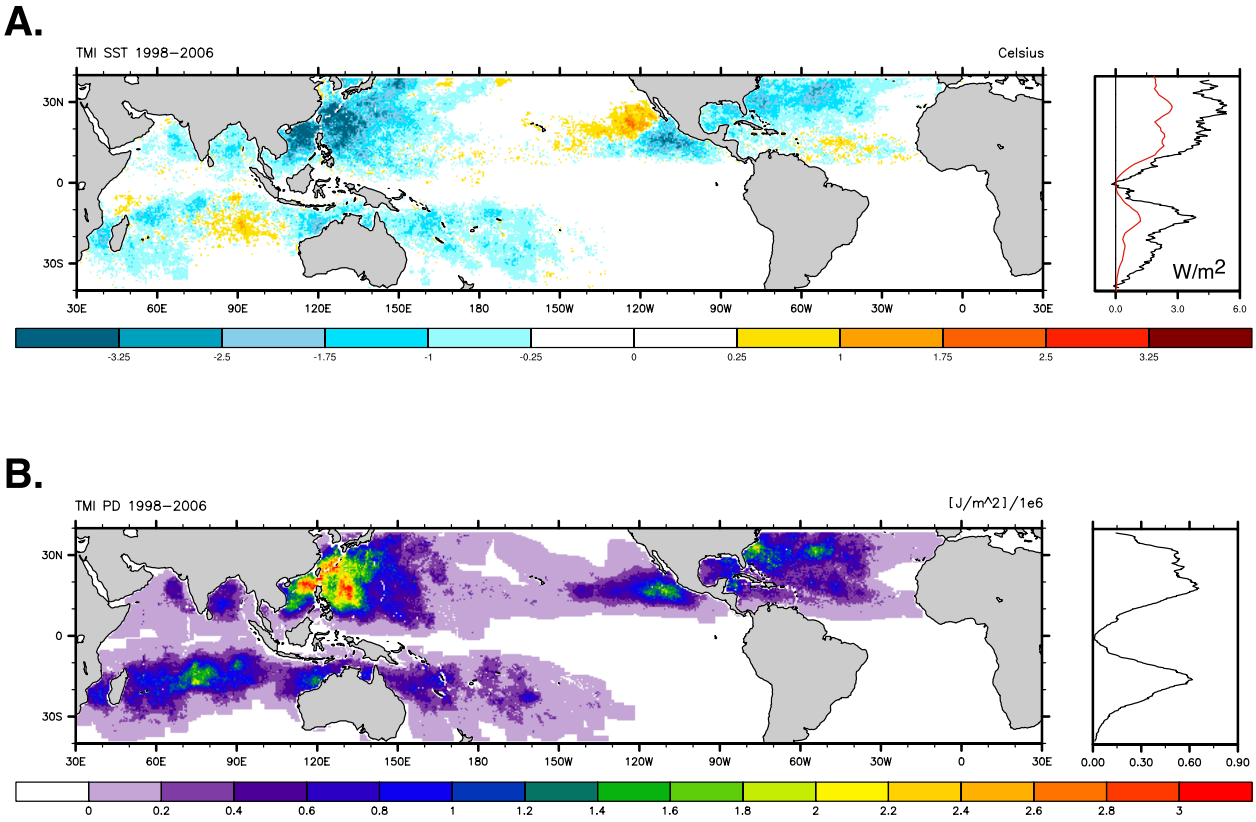

Figure 1. (a) Time average of the annually accumulated, cyclone-induced sea surface temperature anomalies derived from Tropical Rainfall Measuring Mission (TRMM) Microwave Imager (TMI) (1998–2006). (right) The zonally averaged fluxes needed to restore the storm-affected regions over 1 year, assuming the anomalies are uniform to 50 m depth. The black curve depicts TMI and the red curve depicts ERA40 sea surface temperature (shown in SH07). (B) Annually averaged global distribution of cyclone power dissipation (PD) (in units J/m^2 divided by a constant 1×10^6) from TMI 11 GHz surface wind speeds (1998–2006). (right) The zonally averaged PD for storm-affected regions.

Our essential results were not changed, and the year-to-year variability in the regional and global time series was preserved. Therefore, the results shown here utilize a constant footprint domain size of $6^\circ \times 6^\circ$ for all storms, which is consistent with our methods in SH07.

4. Results and Discussion

4.1. Cyclone-Induced Cooling

[22] Figure 1 shows the distributions of the annually integrated cyclone-induced SST anomalies (Figure 1a) and PD (Figure 1b) averaged over the time period 1998 to 2006. Figures 1a and 1b are derived from TMI surface temperature and winds, and the quantities are plotted over TMI's spatial domain (-40° to $+40^\circ$ north). The patterns observed in Figures 1a and 1b are similar, with the largest SST cooling occurring in regions subjected to the most cyclone activity, corresponding to the highest values of annual integrated intensity. Some regions typically experience mild warming associated with passing cyclone events, but analysis suggests this warming is likely a surface feature associated with weak, early season storms and developing cyclones. The large warming region observed in the eastern Pacific is a notable exception to the widespread cooling pattern and is unexplained.

[23] Provided that cooling is driven by vertical mixing as current modeling and observations indicate [*Shay et al.*, 1992, 1998; *Jacob et al.*, 2000; *D'Asaro*, 2003], the spatial similarity between Figures 1a and 1b suggests a positive relationship between integrated intensity and vertical ocean mixing. Consequently, regions experiencing more cyclone activity exhibit increased surface cooling indicative of downward pumping of ocean heat beneath the mixed layer and into the thermocline.

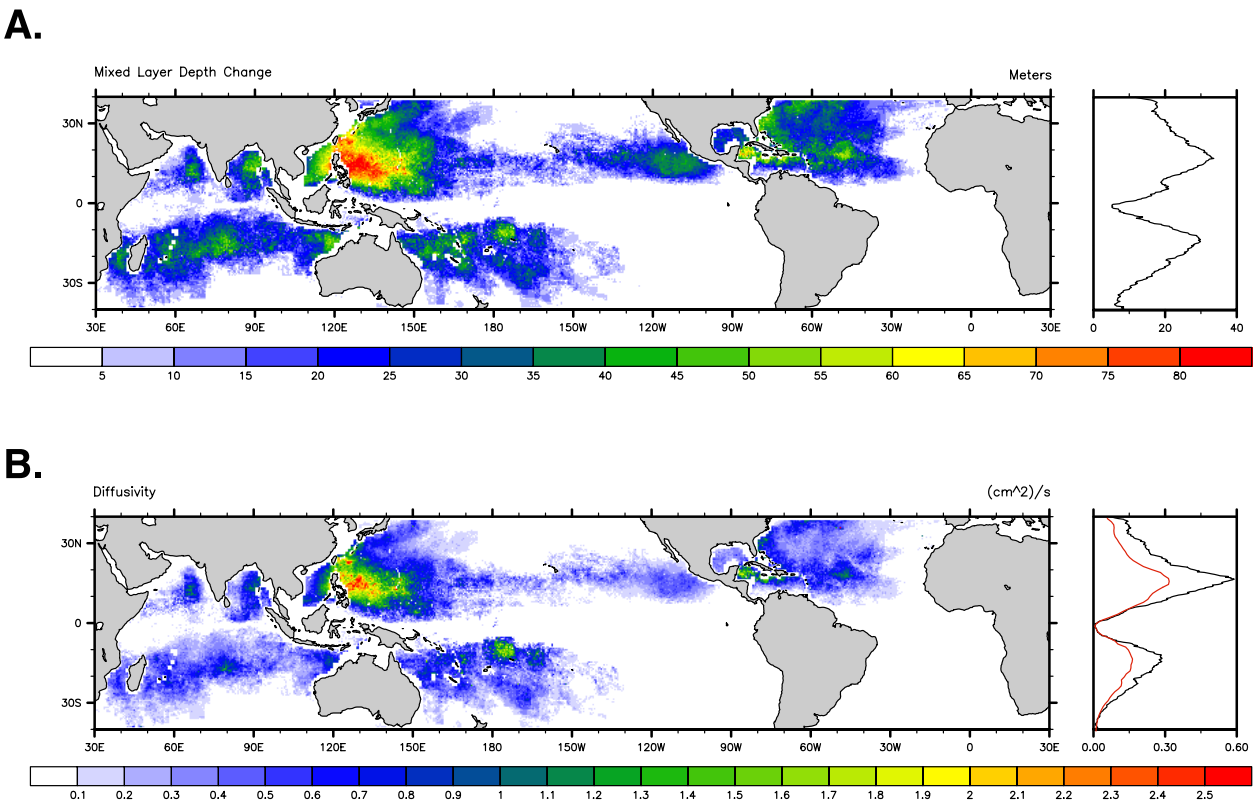

Figure 2. (a) Annually averaged cyclone-induced mixed layer depth changes (1998–2006). Values refer to the increase in mixed layer depth attributable to the single largest cyclone mixing event per year (based on TMI surface temperature anomalies) and averaged over all available years. (right) The zonally averaged mixed layer depth change for storm-affected regions. (b) Annualized vertical diffusivity attributable to cyclone mixing calculated from the mixed layer depth changes shown in Figure 2a, averaged over the years 1998–2006. Diffusivity calculation assumes a mixing timescale of 24 h and that the largest single cyclone mixing event is the only mixing occurring at each point during the year. (right) The zonally averaged diffusivity for the entire domain. The black curve depicts TMI-derived diffusivity and the red curve depicts values derived using ERA40 (shown in SH07).

[24] The distribution of widespread SST cooling over TMI's domain shown in Figure 1a is consistent with previously published results using ERA40 SST and 2 m air temperature (see SH07). Expressed as a surface heat flux (right of Figure 1a), Figure 1a suggests fluxes as large as $\sim$5 W/m^2 annually are needed to restore storm-affected areas to prestorm temperatures (assuming the SST anomaly is uniform to 50 m depth). While spatially consistent with reanalysis, Figure 1a displays an increase in the magnitude of cyclone-induced surface cooling in active storm regions compared to ERA40 and NCEP (see right of Figure 1a). This increase is likely due to the higher spatial and temporal resolutions of TMI compared to reanalysis SST and its ability to sense through clouds [*Wentz et al.*, 2000]. The TMI spatial resolution is 0.25° $\times$ 0.25° and can produce complete global coverage within 2 to 3 days, whereas reanalysis exhibits lower spatial resolution, e.g., 1.125° $\times$ 1.125° for ERA40 and $\sim$1.9° $\times$ 1.9° for NCEP, and SST is weekly averaged after 1981 for both reanalysis data sets. Thus, TMI provides a more accurate representation of short-term SST variations.

[25] Figure 2a displays the calculated annual cyclone-induced mixed layer depth changes averaged over the years 1998 to 2006. These depths define the mixing length scales used to quantify the cyclone contribution to vertical diffusivity shown in Figure 2b. We calculate mixed layer depth change using TMI surface temperature anomalies combined with vertical temperature profiles from the World Ocean Atlas (1998) [*Levitus et al.*, 2000]. We begin by assuming the single largest cyclone-induced cooling event at each location is the only cooling per year, resulting in annual maps of the largest negative temperature anomaly at every storm-affected grid location. We then use vertical temperature profiles (averaged over hurricane season months for each basin) to determine the

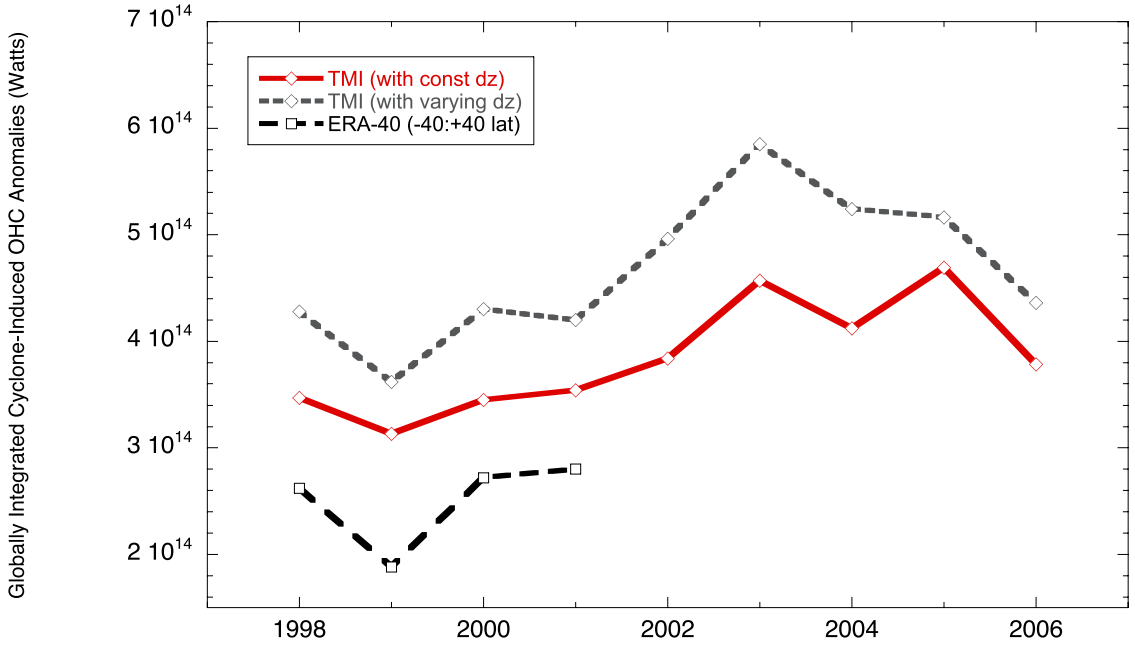

Figure 3. Globally integrated cyclone-induced ocean heat content (OHC) anomalies (represented as annual energy input to the ocean (watts)). OHC anomalies are calculated from sea surface temperature anomalies as discussed in section 3. Red curve denotes TMI (−40° to + 40° latitude) assuming constant mixing depths of 50 m. The dashed gray curve represents TMI utilizing mixing depths calculated by combining surface temperature anomalies with cyclone season-averaged vertical temperature profiles. The dashed black curve represents OHC derived from ERA40, which represents a subset corresponding to the TMI region (−40° to +40° latitude).

length scale of the mixing, i.e., depth from which upwelling occurs. In other words, the mixed layer depth change is the depth to which mixing must occur to achieve the largest observed surface temperature anomalies per year. This method for calculating cyclone mixing depth reflects a somewhat simplified approach, in that we do not account for transient increases in regional SST occurring prior to storm passage that are not captured in the seasonal vertical temperature profiles. Our mixing depth estimates range from 10 m for small temperature anomalies to over 80 m for strong mixing events. Such increases in mixed layer depths at low latitudes have been shown to significantly impact meridional overturning strength and poleward ocean heat flux [*Huang et al.*, 2007]. We note that this mixing assumption is conservative in the sense that some regions (e.g., in the west Pacific) may experience several large mixing events in a given year; therefore mixing may be stronger than indicated from only the single largest event [*Liu et al.*, 2008].

[26] The mixed layer depth changes shown in Figure 2a are used to estimate effective vertical diffusivities attributable to cyclone mixing shown in Figure 2b. These diffusivities are calculated assuming cyclones mix this thickness of water shown in Figure 2a on a characteristic e-folding timescale of 24 h (consistent with observations) and that only one mixing event occurs at each location per year. The map of vertical diffusivities shows maxima in regions with pronounced cyclone activity (Figure 1b). Figure 2b (right) shows the effective diffusivity averaged zonally across all ocean regions for TMI (black curve) and ERA40 (red curve; discussed in SH07). The average TMI-derived diffusivities are around twice the typical values from ERA40. The diffusivities shown in Figure 2b are similar to recent findings [*Korty et al.*, 2008] and are consistent with background values currently used in ocean general circulation models. These results further suggest the conjecture that vertical mixing missing from the current generation of ocean model simulations may be attributable to transient extreme mixing events such as tropical cyclones.

[27] We show the globally integrated time series for cyclone-induced OHC anomalies in Figure 3. Assuming steady state, anomalies are represented as an annual heat transport (in watts) and the time series covers the TMI data record from 1998 to 2006. We show anomalous OHC calculated using a constant mixing depth (50 m), as well as OHC from combining the surface temperature anomalies with the vertical temperature profiles to approxi-

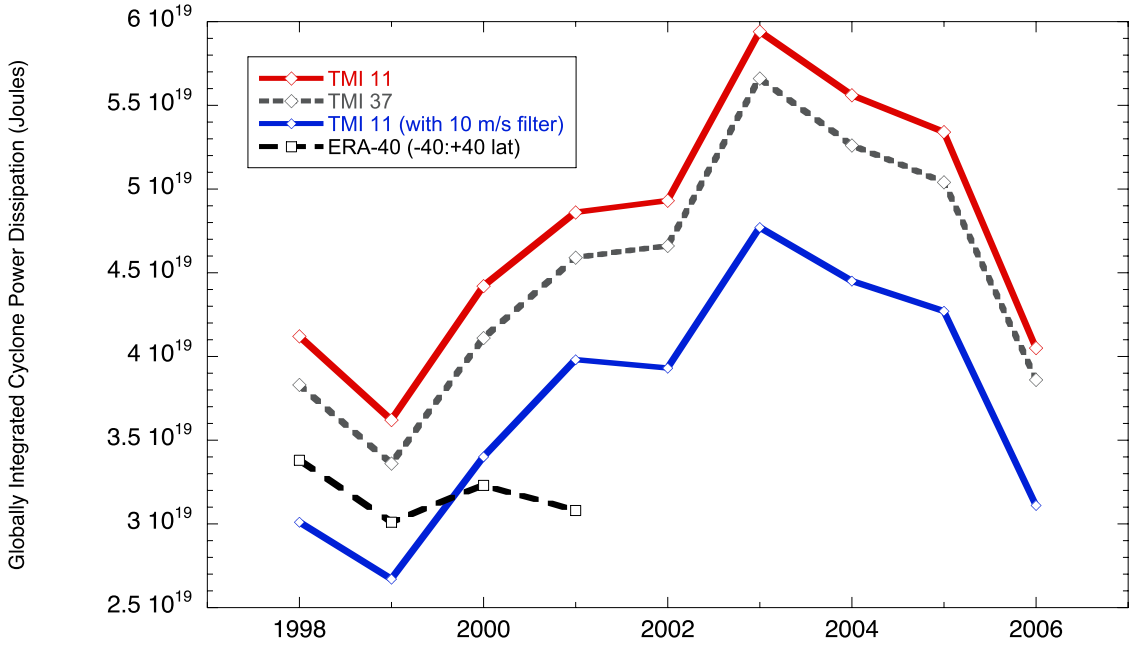

Figure 4. Globally integrated cyclone-induced power dissipation (PD) (in joules). TMI PD (−40° to + 40° latitude) is shown for winds retrieved using the 11 GHz (red curve) and 37 GHz (dashed gray curve) channels. Blue curve represents PD from the TMI 11 GHz channel with a 10 m/s wind filter applied (see text for discussion). The dashed black curve represents a subset of ERA40 corresponding to the TMI region (−40° to +40° latitude).

mate spatially varying annual mixed layer depth changes (see section 3.3). ERA40-derived OHC anomalies are shown for years overlapping with TMI (1998–2001). We have scaled the ERA40 OHC to the same spatial domain as TMI (−40° to +40° latitude) for comparison. Results show a similar trend between the two series with ERA40 underrepresenting the anomalous OHC signal compared to TMI. The TMI series that utilizes the constant mixing depths shows a 35% increase in OHC compared to ERA40, while OHC calculated from varying mixing depths shows roughly a ∼60% increase compared to ERA40, with peak values reaching near 0.6 PW (1PW = 10^{15} W). These results suggest SH07's estimation of the contribution of cyclone-induced mixing to global ocean heat transport may be too low, at least toward the end of the ERA40 record comparable to TMI.

[28] As discussed in the methods, this simplified calculation for cyclone-induced anomalous OHC assumes that vertical ocean mixing accounts for all of the temperature anomalies observed at the surface. *Trenberth and Fasullo* [2007] have recently suggested that tropical cyclones may substantially contribute to the atmospheric poleward heat flux, and they estimate that ∼0.5 J a^{-1} of heat is lost from the ocean through surface fluxes by cyclone-induced latent heating of the atmosphere. This corresponds to 0.17 PW, or roughly 28% of our peak estimates. Thus, while our calculations serve as a first-order estimate of the heat uptake by the oceans due to tropical cyclone mixing, further research is clearly needed to fully understand the effect of these events on heat convergence/transport for the oceans and atmosphere.

4.2. Cyclone Integrated Intensity

[29] Figure 4 shows the globally integrated time series for cyclone PD from TMI and ERA40. Annually averaged PD for the 11 GHz TMI sensor with no wind filter is 5 × 10^{19} J. In Figure 4, all TMI wind records reproduce similar PD time series, except the magnitude of PD from the 37 GHz winds is less than the 11 GHz wind-derived series by an offset of ∼0.4 × 10^{19} J. We do not attempt to resolve differences arising from the use of multiple TMI channels here, but we note the larger magnitude PD derived from 11 GHz winds is likely due to the higher transparency of nonprecipitating clouds at the low end of TMI's frequency range.

[30] As an example of our sensitivity analysis described in the methods section, we have plotted the TMI PD time series for the 11 GHz channel with a 10 m/s filter applied (Figure 4). The portions of the cyclone wind field with speeds less

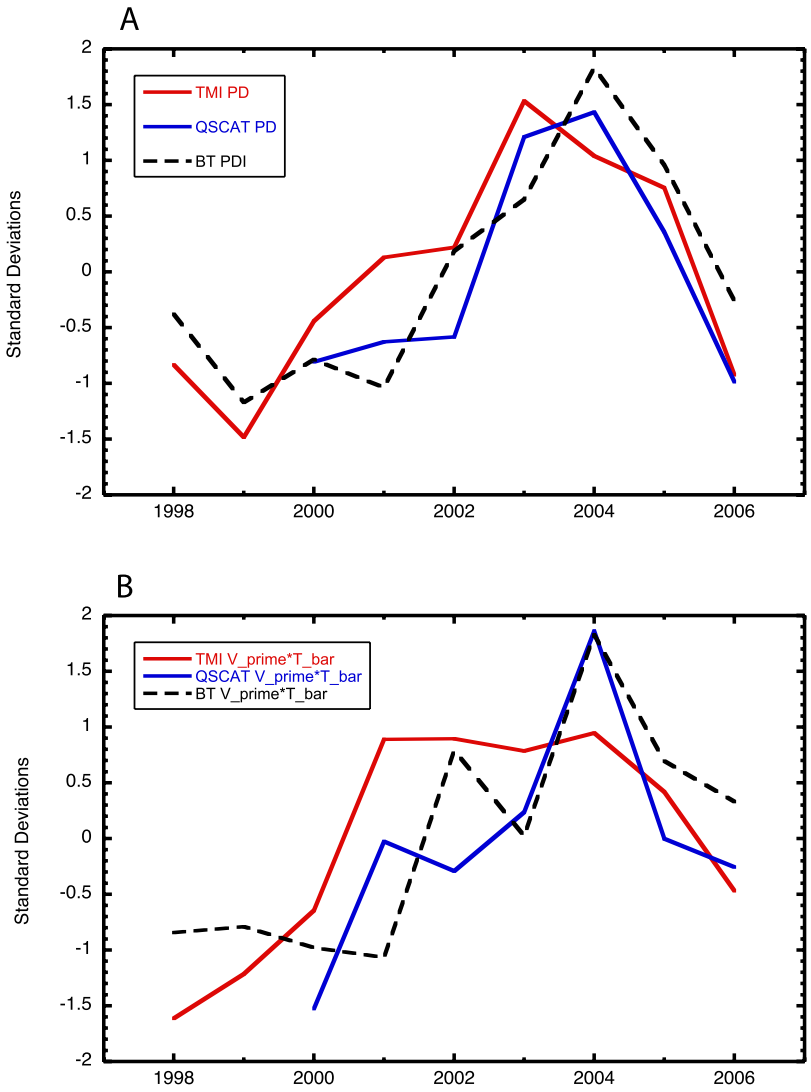

Figure 5. (a) Globally integrated cyclone-induced power dissipation (PD) from TMI (red curve) and QuikScat (blue curve), and Best Track (BT) power dissipation index (dashed black curve) for the period 1998–2006. All series are normalized by subtracting the time mean and dividing by the respective standard deviation. (b) Partial results from the Reynold's decomposition of the globally integrated power dissipation (PD) for TMI (red curve) and QuikScat (blue curve), and the power dissipation index from the Best Track maximum sustained surface wind estimates (dashed black curve). All curves represent the wind-sensitive components of PD for TMI and QuikScat, and PDI for Best Track, and all curves are normalized as in Figure 5a.

than 10 m/s have been removed from the PD integral. While the magnitude of the filtered PD is less than PD containing the entire wind field, the trend and variability is very similar. We performed similar exercises utilizing varying wind speed filters and footprint domain sizes, and the variability within all regional and global PD time series remained largely unchanged. Furthermore, efforts to constrain the magnitude of global PD can be facilitated by applying this type of wind filter to a high-resolution wind data set in order to achieve a more realistic representation of the cyclone winds (using a larger footprint size). Such efforts are useful for estimating the amount of surface wind energy available for ocean mixing.

[31] A subset of ERA40 PD consistent with the TMI spatial domain is plotted in Figure 4. On average, we find that TMI PD is ~30% greater than ERA40 over the same spatial domain (−40° to +40° latitude) for overlapping years (1998–2001). Annually averaged PD calculated from QuikScat is calculated to be $\sim 1.7 \times 10^{20}$ J. This corresponds to more than a threefold increase in globally integrated, annual PD for QuikScat compared to TMI for the overlapping years (2000–2006).

[32] PD is often approximated as the Power Dissipation Index (PDI),

$$PDI = \int |V_m|^3 dt$$

which is proportional to the cube of the maximum sustained surface wind (V_m) and is integrated over the lifetime of the storm. PDI differs from PD, where the latter quantity is spatially integrated over the entire wind field. Previous results [*Sriver and Huber*, 2006, 2007a, 2007b] indicate that PDI is a reasonable approximation to PD and adequately reproduces low frequency variability in globally integrated cyclone intensity. Figure 5a shows a comparison between global PD from TMI and QuikScat, along with global PDI derived from Best Track winds. The TMI and Best Track time series span 1998 to 2006, while the QuikScat time series is from 2000 to 2006. We normalize all curves by subtracting the time mean and dividing by the standard deviation.

[33] Figure 5a shows general agreement between TMI PD, QuikScat PD, and Best Track PDI, though one major difference appears to be the Best Track and QuikScat time series are offset from TMI during much of the time period. Best Track and QuikScat underrepresent the upward shift in integrated intensity from 1999 to 2003 observed in TMI, and the Best Track and QuikScat peaks occur 1 year after the associated peak in TMI.

[34] We attempt to explain the differences in the curves shown in Figure 5a by performing a Reynold's decomposition on the quantities. We define V and T to be the wind-sensitive and track-sensitive terms of PD (or PDI), and we separate V and T into the time mean plus annual perturbation ($V = \overline{V} + V'$ and $T = \overline{T} + T'$). Using this formalism, the product VT can be written as the sum of the time-averaged product ($\overline{VT}$) plus the wind-sensitive ($V'\overline{T}$) and the time-sensitive ($\overline{V}T'$) components. The higher-order term ($V'T'$) is ignored (see *Sriver and Huber* [2007a] for a more complete description). The main point of this analysis is to focus on the part of the PD trend that reflects wind intensity changes [*Sriver and Huber*, 2007a; *Maue and Hart*, 2007].

[35] Figure 5b shows the results of the Reynold's decomposition for globally integrated PD from TMI and QuikScat, and PDI from Best Track shown in Figure 5a. We only compare the wind-sensitive component of integrated intensity ($V'\overline{T}$), since the same track information (location and time) is used for all three quantities (thus the shapes of the time-sensitive components ($\overline{V}T'$) are identical). All quantities are normalized by their respective standard deviations as in Figure 5a. Figure 5b exhibits general agreement between wind-sensitive components of QuikScat PD and Best Track PDI, with both time series peaking in 2004. The main difference appears to be attributable to the wind-sensitive component of TMI PD. TMI does not appear to reproduce the variability observed in the other two series, overestimating the initial upward trend and underestimating the peak in 2004. The difference in the curves shown in Figure 5b suggests that TMI cyclone wind representation is inconsistent with QuikScat and Best Track winds, leading to the discrepancies in the variability shown in Figure 5a. This difference is likely due to the underrepresentation of the magnitude of TMI cyclone wind fields compared to QuikScat and Best Track estimates or possible instrument bias within TMI.

[36] To investigate regional biases between TMI, QuikScat, and Best Track, we perform basin-by-basin comparisons of PDI and PD in Figures 6 and 7. In Figure 6, we compare PDI derived from TMI and Best Track for the period 1998 to 2006, and QuikScat for the period 2000 to 2006 for five different regions: the northern Atlantic (Figure 6a), the northeastern Pacific (Figure 6b), the northern Indian (Figure 6c), the Southern Hemisphere (Figure 6d), and the northwestern Pacific (Figure 6e). In addition, we have plotted the recently constructed PDI time series from the University of Wisconsin-Madison National Climatic Data Center (NCDC) for the northern Atlantic, northeastern Pacific, and northwestern Pacific regions [*Kossin et al.*, 2007]. NCDC PDI is calculated between −45° and +45° latitude and only includes events over water (similar to TMI, except the domain extends to 45° latitude rather than 40° latitude). All time series are normalized as in Figure 5.

[37] Figure 6 shows TMI and QuikScat PDI generally agree. NCDC PDI and Best Track PDI closely agree for the Atlantic and northwestern Pacific regions and for the majority of the northeastern Pacific time series, with the exception being in the portion of the northeastern Pacific record from 1998 to 2001. During these 3 years, the NCDC PDI agrees with TMI more closely than Best Track, possibly suggesting biases in the Best Track winds during this period. In the Atlantic region, TMI PDI is underrepresented with respect to Best Track and NCDC for the years 1998–2000

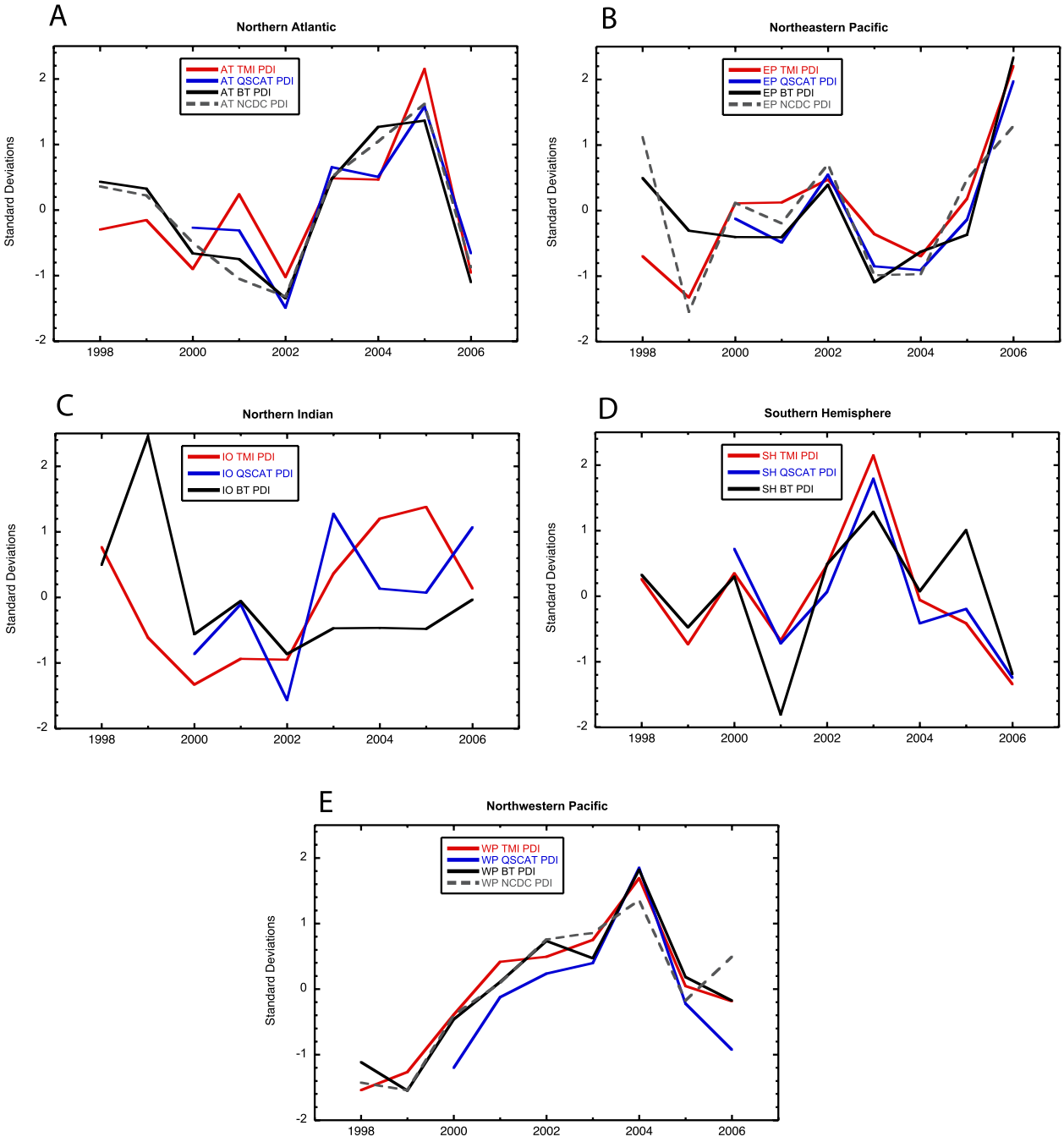

Figure 6. Tropical cyclone power dissipation index (PDI) derived from TMI (red curves), QuikScat (blue curves), and Best Track (black curves) for (a) Northern Hemisphere Atlantic (AT); (b) Northern Hemisphere eastern Pacific (EP); (c) Northern Hemisphere Indian Ocean (IO); (d) Southern Hemisphere (SH); (e) Northern Hemisphere western Pacific (WP). PDI results from the University of Wisconsin-Madison National Climatic Data Center (NCDC) [*Kossin et al.*, 2007] (dashed gray curves) are plotted for the AT, EP, and WP basins. All series are normalized by subtracting the time mean and dividing by the standard deviation.

and 2004, and it is overrepresented in 2001–2002. TMI and QuikScat generally agree in the Atlantic region throughout the record. The poorest agreement between TMI, QuikScat, and Best Track PDI occurs in the northern Indian Ocean. However, this region contributes the least to globally integrated intensity, with typical yearly values of PD an order of magnitude less than for the more active South-

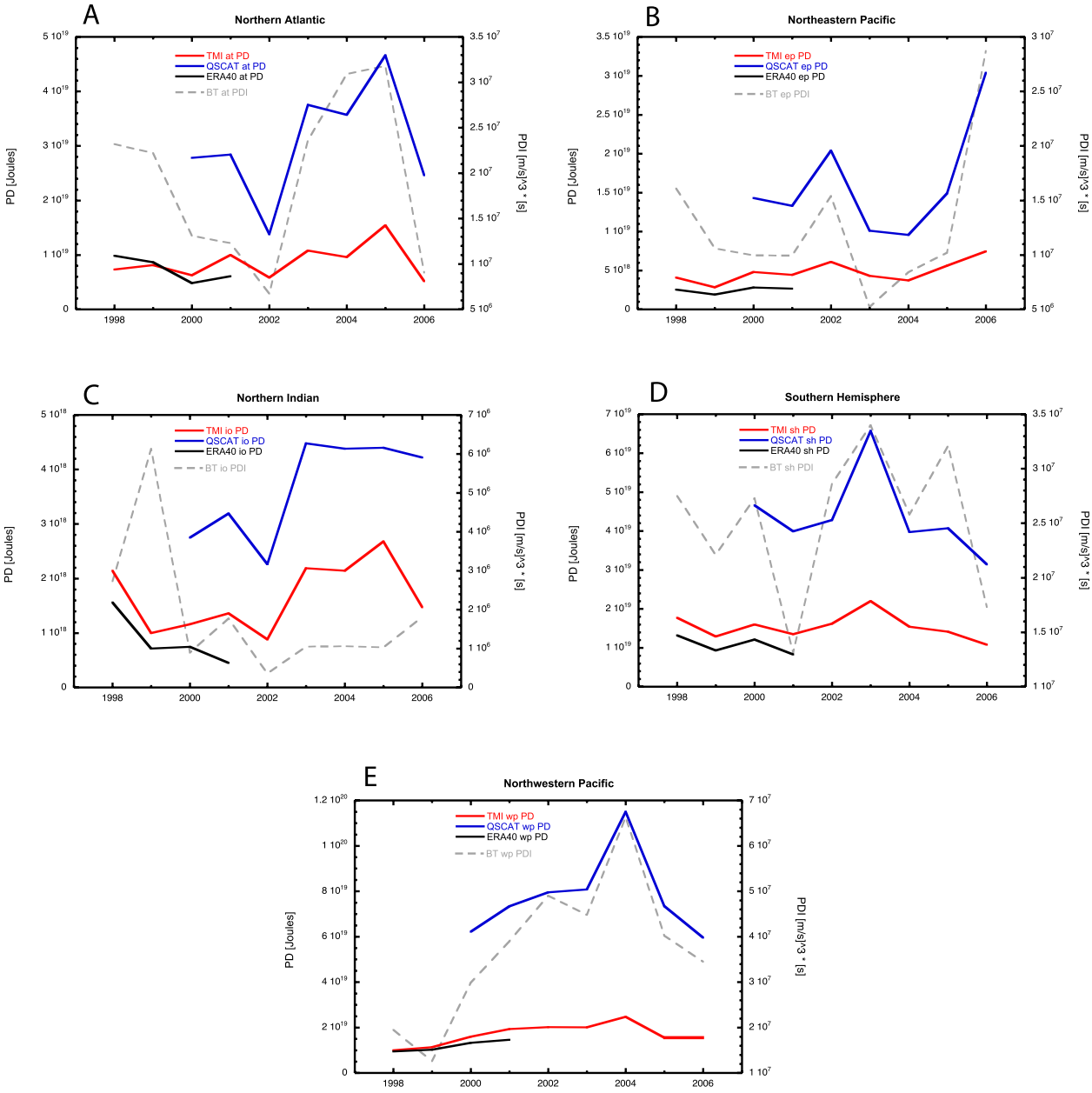

Figure 7. Tropical cyclone power dissipation (PD) from TMI (red curves), QuikScat (QSCAT, blue curves), ERA40 (black curves), and the Power Dissipation Index (PDI) from Best Track estimates (dashed gray curves) for (a) Northern Hemisphere Atlantic (AT); (b) Northern Hemisphere eastern Pacific (EP); (c) Northern Hemisphere Indian Ocean (IO); (d) Southern Hemisphere (SH); (e) Northern Hemisphere western Pacific (WP). PD is plotted on the left y axis (in joules), and PDI is plotted on the right y axis (in $(m/s)^3(s)$).

ern Hemisphere and northwestern Pacific regions. Therefore, discrepancies between quantities in this region do not propagate onto the globally integrated time series. While year-to-year variability is consistent between all quantities in the Southern Hemisphere region, TMI and QuikScat overrepresent PDI during the middle of the record (2001 and 2003), and it is underrepresented in 2005. The northwestern Pacific region exhibits good agreement between all quantities.

[38] To illustrate the differences in PD estimated from different data sources, we plot regional PD calculated from ERA40, TMI, and QuikScat in Figure 7 (left axis). Also shown is PDI from Best Track winds plotted on the right axis. Figure 7

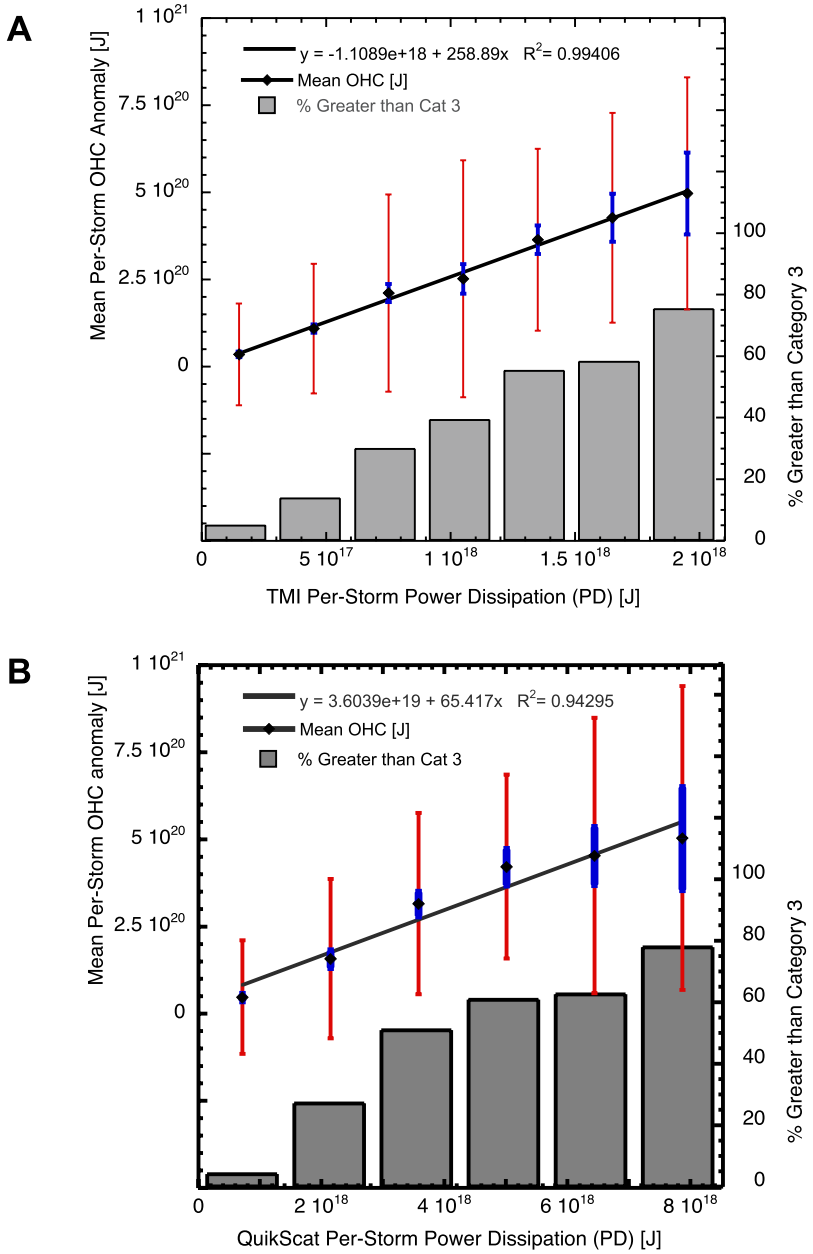

Figure 8. Mean per-storm ocean heat content (OHC) anomalies from TMI (black points) as a function of the per-storm power dissipation (PD) calculated using TMI (Figure 8a) and QuikScat (Figure 8b) winds. OHC and PD are both measured in joules. Cyclone PD is divided into equally spaced bins that span most of the range observed within TMI and QuikScat, and the mean cyclone-induced anomalous OHC is calculated for each bin. Red error bars represent ±1 standard deviation, and blue error bars represent ± the standard error. The black line represents the linear fit for mean per-storm OHC as a function of binned PD. The bar graphs represent the percentage of storms within each bin that reached category 4 or higher according to the maximum sustained surface winds speeds within the Best Track storm information.

shows general agreement between QuikScat, TMI, and ERA40 for overlapping years, with QuikScat reflecting higher magnitude and variability. While annual, globally integrated PD from TMI is 30% higher than ERA40 (discussed earlier), globally integrated PD from QuikScat is estimated to be ~3.5 times greater than TMI PD on average for years overlapping between data sets. This large difference in magnitude reflects QuikScat's ability to more accurately sense wind speeds within tropical cyclones compared to both ERA40 and TMI.

4.3. PD/OHC Feedbacks

[39] To establish the dependence of cyclone-induced ocean heat convergence on cyclone PD, we calculated the storm-integrated OHC anomalies and PD for all Best Track cyclone events occurring globally from 1998 to 2006 for TMI (Figure 8a) and 2000 to 2006 for QuikScat (Figure 8b). In Figure 8a, we separated 811 events into seven equally spaced bins of PD spanning nearly the full range of values returned by TMI. Ten storms with PD values exceeding the upper limit (seventh bin) were excluded due to the small sample size of additional bins. For each PD bin, we calculated the respective mean, standard deviation, and standard error for the corresponding population of storm-induced anomalous OHC calculated from TMI-derived storm integrated SST anomalies. We preformed linear regression analysis that yielded a positive, linear relationship between mean per-storm anomalous OHC and binned PD (black line).

[40] We performed similar analysis comparing per-storm PD from QuikScat (Figure 8B) with per-storm anomalous OHC from TMI SST for 622 events from 2000 to 2006. We separated the events into six equally spaced bins of PD ranging from 1.4×10^{18} J to 8.6×10^{18} J, with 14 events excluded due to the small sample size of additional bins. We decreased the number of bins from seven (Figure 8a) to six (Figure 8b) in order to better retain a more consistent sample size at the high end of the PD range for QuikScat winds. Results were closely similar to the TMI-derived relationship shown in Figure 8a, and a linear regression yielded a correlation of $R^2 = 0.94$ between per-storm PD and per-storm anomalous OHC, consistent with the relationship observed in Figure 8a. The observed relationship between per-storm PD and anomalous OHC in Figure 8 suggests that storms with larger PD values (e.g., stronger winds, larger area, and/or longer lasting) lead to greater surface cooling, vertical mixing, and downward heat pumping within the tropical oceans.

[41] Error estimates for per-storm anomalous ocean heat content shown in Figure 8 are performed in two ways. The red lines denote ±1 standard deviation for the OHC values calculated within each PD bin, and the blue lines represent the standard error for the binned data. Given that the majority of cyclone events occur near the low end of the PD range, i.e., most do not reach major hurricane status, it is not surprising that the standard error is relatively low for small PD storms since the sample size is large there. The standard error increases with increasing PD as the number of events decreases. On the other hand, the relatively larger error estimated using the standard deviation reflects the spread of the sampled data within each PD bin.

[42] Since PD is the convolution of surface wind speed, duration, and size, the relative contribution of each component to vertical mixing is not clear, though they are all likely important. To better understand the relationship between per-storm PD and the more usual indices of storm intensity, we calculate the percentage of cyclones in each bin that achieved category status greater than 3 (bar graphs in Figure 8) according to the maximum sustained surface winds contained in the Best Track information. The bar graphs display a clear upward trend, suggesting that higher category storms typically account for larger integrated intensities and more vertical ocean mixing. Given that ocean mixing is normally associated with a threshold in which the critical gradient Richardson number is exceeded, it is quite likely that it is not just the spatially integrated portion of PD which determines the amount of mixing but also the duration of strong winds. This latter component is suggested by the increase in OHC with increasing percentage of strong cyclone winds. On average (but not necessarily on a storm-by-storm basis), PD is highly correlated with per-storm intensity, and it is a reasonable indicator for cyclone-induced vertical ocean mixing and OHC anomalies.

[43] The OHC trend and the associated error shown in Figure 8 offer additional insight into the cyclone-induced climatic feedback hypothesis. The low end of the PD range can be assumed to represent ocean surface temperature variability in the presence of negligible storm-induced vertical mixing, i.e., the null hypothesis. In other words, the lowest PD bin provides a quantitative estimate of the mean and range of values that would occur if we applied our sampling over an ocean characterized by noise. Therefore, if OHC is not a function of PD, then OHC should not fall outside the range of variability for zero magnitude storms or storms with weak mixing. The error for the low end of the OHC function describes the natural surface temperature variability with no important effect on tropical cyclones or ocean temperature. Given that the high end of the PD range yields OHC anomaly values well outside the error limits within the null hypothesis region, the positive dependence of OHC on PD is supported with both TMI and QuikScat data.

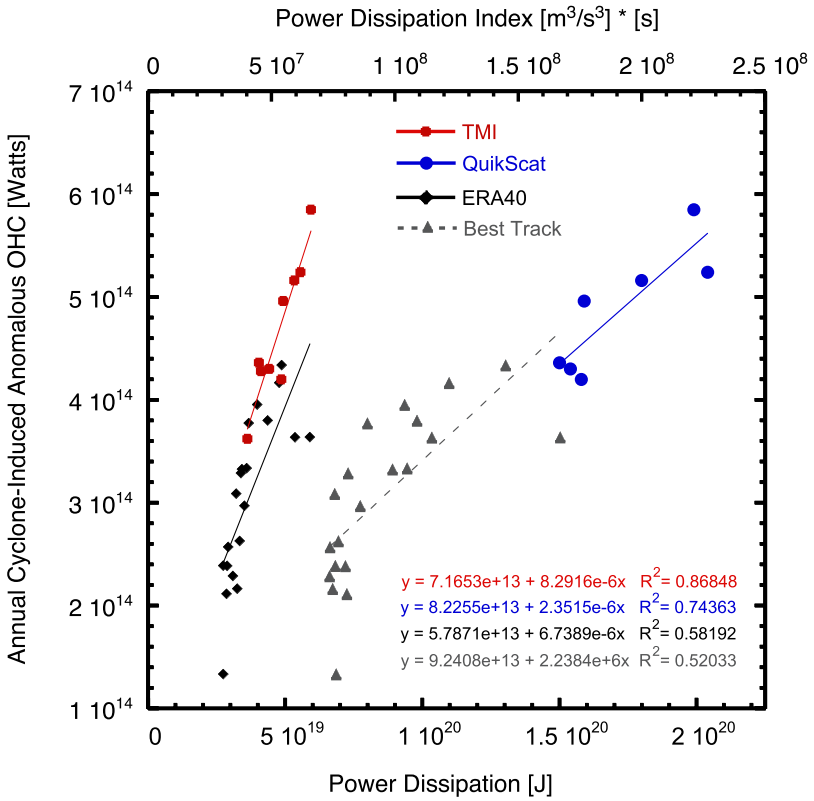

Figure 9. Globally integrated, annual cyclone-induced anomalous OHC versus PD for TMI (red), QuikScat (blue), ERA40 (black), and Best Track PDI (gray). Because QuikScat and Best Track do not contain temperature data, SST from TMI and ERA40 is used for the QuikScat and Best Track data points, respectively. The years shown for ERA40 and Best Track are 1982–2001. The years for TMI are 1998–2006 and QuikScat are 2000–2006.

[44] The positive relationship shown in Figure 8 is also observed for globally integrated PD and OHC. Figure 9 represents a scatterplot of the globally integrated, annual cyclone-induced anomalous OHC as a function of globally integrated, annual PD for the data sources: ERA40, TMI, and QuikScat. Also shown is globally integrated, annual PDI from Best Track (plotted along the upper x axis). Anomalous OHC is calculated from storm-induced SST anomalies and is represented here as annual transport, equivalent to the annual amount of ocean heat pumped vertically by cyclones and subsequent steady state lateral transport. Since ERA40 and TMI are the only data sources containing temperature information, TMI and ERA40 derived OHC is used for plotting QuikScat PD and Best Track PDI, respectively. The years shown for ERA40 PD and Best Track PDI reflect the period where ERA40 uses weekly SST fields rather than monthly (1982–2001) [*Uppala et al.*, 2005].

[45] The linear regressions in Figure 9 reflect the general positive relationship between globally integrated PD and cyclone-induced anomalous OHC. Scaling arguments and previous numerical simulations have suggested a 3/2 power law dependence of the power expended by wind-driven ocean mixing (PD) on poleward ocean heat flux (or anomalous OHC) [*Emanuel*, 2002; *Scott and Marotzke*, 2002]. Our results do not support a nonlinear relationship between PD and OHC, but our analysis is limited by the availability of reliable data. We do show these quantities to be strongly positive correlated, suggesting the nonlinear scaling dependence is plausible.

[46] Figures 8 and 9 both suggest that storms with larger integrated intensities will likely lead to increased vertical mixing and cyclone-induced anomalous OHC. Thus, given the strong correlation between low-frequency cyclone variability and surface temperature, future increases in tropical SST will likely be accompanied by increased integrated cyclone activity, resulting in enhanced vertical ocean mixing and positive anomalous OHC beneath the mixed layer. Whether this OHC is eventually expressed as increased poleward

ocean heat transport, as has been conjectured, is impossible to assess with our current methodology.

5. Conclusions and Implications

[47] We utilized SST and surface wind data from TMI for 1998 to 2006, along with QuikScat surface wind data from 2000 to 2006, to present a global representation of cyclone-induced surface temperature anomalies and power dissipation. These techniques offer a unique opportunity to analyze surface temperature and winds within cyclone environments using up-to-date, high-resolution, and independent data sets. We find that cyclone-induced vertical ocean heat pumping is ~35% higher than previous estimates based on reanalysis, and new methodology, which utilizes seasonal vertical temperature profiles for determining mixing depths, suggests heat pumping may be ~60% higher than previously published estimates. Furthermore, the resulting effective vertical diffusivities are roughly twice the size of those calculated in SH07. Power dissipation estimates are also significantly higher, with averages of $\sim 5 \times 10^{19}$ J and $\sim 1.7 \times 10^{20}$ J from TMI and QuikScat, respectively. These estimates reflect a 30% increase in globally integrated, annually averaged TMI PD compared to ERA40 for overlapping years and more than a threefold increase in QuikScat PD compared to TMI. Results suggest the underrepresentation of surface quantities in cyclone conditions for ERA40 compared to the more highly resolved TMI, as well as an underestimation of cyclone winds in TMI compared to QuikScat.

[48] We show a positive relationship between cyclone-induced OHC anomalies and PD on a per-storm basis, with the higher-category storms accounting for a larger contribution to global PD and anomalous OHC. This positive relationship holds for globally integrated, annual PD and anomalous OHC. These results support the hypothesis for cyclone-induced climatic feedbacks, where increases in globally integrated cyclone intensity associated with warming surface temperatures may provide a positive feedback on poleward ocean heat transport through enhanced vertical ocean mixing. In other words, more power dissipated at the surface by cyclone winds infers more turbulent ocean mixing and vertical heat pumping, which may influence oceanic heat convergence and transport since ocean heat transport is sensitive to diapycnal mixing in the tropics. This cyclone-induced mixing may be the "missing" mixing in today's generation of ocean general circulation models. These models currently prescribe background diffusivity values similar to those estimated here that we attribute to transient cyclone mixing. In order to reproduce past climate variability and accurately project future climate change scenarios, a better representation of cyclone mixing (and the associated feedback mechanisms) needs to be included in climate simulations.

Acknowledgments

[49] We gratefully acknowledge K. Emanuel and two anonymous reviewers for comments and suggestions that greatly improved this manuscript. We thank Wei Wang for a preprint of the *Liu et al.* [2008] manuscript, K. Emanuel for supplying hurricane track data, and J. Kossin for contributing the UW/NCDC PDI time series. TMI data are produced by Remote Sensing Systems and sponsored by the NASA Earth Science REASoN DISCOVER Project. QuikScat data are produced by Remote Sensing Systems and sponsored by the NASA Ocean Vector Winds Science Team. TMI and QuikScat data are available at www.remss.com. NODC_WOA98 data were provided by the NOAA/OAR/ESRL PSD, Boulder, Colorado, USA, from their Web site at http://www.cdc.noaa.gov. ERA40 data were provided by the Data Support Section of the Scientific Computing Division at the National Center for Atmospheric Research. NCAR is supported by grants from the National Science Foundation. This work was supported by grant NSF ATM 0741797 to MH. The authors also acknowledge the use of the NCAR Command Language (NCL) in most of the data analysis and visualization herein.

References

Black, P. G., et al. (2007), Air-sea exchange in hurricanes: Synthesis of observations from the coupled boundary layer air-sea transfer experiment, *Bull. Am. Meteorol. Soc.*, *88*, 357–374, doi:10.1175/BAMS-88-3-357.

Bugnion, V., C. Hill, and P. H. Stone (2006), An adjoint analysis of the meridional overturning circulation in a hybrid coupled model, *J. Clim.*, *19*, 3751–3767, doi:10.1175/JCLI3821.1.

Chelton, D. B., and M. H. Freilich (2005), Scatterometer-based assessment of 10-m wind analyses from the operational ECMWF and NCEP numerical weather prediction models, *Mon. Weather Rev.*, *133*, 409–429, doi:10.1175/MWR-2861.1.

D'Asaro, E. A. (2003), The ocean boundary layer below Hurricane Dennis, *J. Phys. Oceanogr.*, *33*, 561–579, doi:10.1175/1520-0485(2003)033<0561:TOBLBH>2.0.CO;2.

Elsner, J. B., et al. (2000), Spatial variations in major U.S. hurricane activity: Statistics and a physical mechanism, *J. Clim.*, *13*, 2293–2305, doi:10.1175/1520-0442(2000)013<2293:SVIMUS>2.0.CO;2.

Emanuel, K. A. (2001), The contribution of tropical cyclones to the oceans' meridional heat transport, *J. Geophys. Res.*, *106*, 14,771–14,782, doi:10.1029/2000JD900641.

Emanuel, K. A. (2002), A simple model of multiple climate regimes, *J. Geophys. Res.*, *107*(D9), 4077, doi:10.1029/2001JD001002.

Emanuel, K. A. (2005), Increasing destructiveness of tropical cyclones over the past 30 years, *Nature*, *436*, 686–688, doi:10.1038/nature03906.

Emanuel, K. A., R. Sundararajan, and J. William (2008), Hurricanes and global warming: Results from downscaling IPCC AR4 simulations, *Bull. Am. Meteorol. Soc.*, *89*, 347–367.

Gentemann, C. L., F. J. Wentz, C. A. Mears, and D. K. Smith (2004), In situ validation of Tropical Rainfall Measuring Mission microwave sea surface temperatures, *J. Geophys. Res.*, *109*, C04021, doi:10.1029/2003JC002092.

Goldenberg, S. B., et al. (2001), The recent increase in Atlantic hurricane activity: Causes and implications, *Science*, *293*, 474–479, doi:10.1126/science.1060040.

Holland, G. J. (2007), Misuse of landfall as a proxy for Atlantic tropical cyclone activity, *Eos Trans. AGU*, *88*(36), 349–350.

Holland, G. J., and P. J. Webster (2007), Heightened tropical cyclone activity in the North Atlantic: Natural variability or climate trend?, *Phil. Trans. R. Soc. London, Ser. A*, *365*, 2695–2716, doi:10.1098/rsta.2007.2083.

Hoshino, S., and T. Nakazawa (2007), Estimation of tropical cyclone's intensity using TRMM/TMI brightness temperature data, *J. Meteorol. Soc. Jpn.*, *85*, 437–454, doi:10.2151/jmsj.85.437.

Huang, R. X., C. J. Huang, and W. Wang (2007), Dynamical roles of mixed layer in regulating the meridional mass/heat fluxes, *J. Geophys. Res.*, *112*, C05036, doi:10.1029/2006JC004046.

Jacob, S. D., et al. (2000), The 3-D oceanic mixed layer response to Hurricane Gilbert, *J. Phys. Oceanogr.*, *30*, 1407–1429, doi:10.1175/1520-0485(2000)030<1407:TOMLRT>2.0.CO;2.

Korty, R. L., K. A. Emanuel, and J. R. Scott (2008), Tropical cyclone-induced upper-ocean mixing and climate: Application to equable climates, *J. Clim.*, *21*, 638–654, doi:10.1175/2007JCLI1659.1.

Kossin, J. P., K. R. Knapp, D. J. Vimont, R. J. Murnane, and B. A. Harper (2007), A globally consistent reanalysis of hurricane variability and trends, *Geophys. Res. Lett.*, *34*, L04815, doi:10.1029/2006GL028836.

Kummerow, C., W. Barnes, T. Kozo, J. Shiue, and J. Simpson (1998), The tropical rainfall measuring mission (TRMM) sensor package, *J. Atmos. Oceanic Technol.*, *15*, 809–817, doi:10.1175/1520-0426(1998)015<0809:TTRMMT>2.0.CO;2.

Landsea, C. W. (2007), Counting Atlantic tropical cyclones back to 1900, *Eos Trans. AGU*, *88*(18), 197.

Landsea, C., et al. (1999), Atlantic basin hurricanes: Indices of climatic changes, *Clim. Change*, *42*, 89–129, doi:10.1023/A:1005416332322.

Levitus, S., J. I. Antonov, T. P. Boyer, and C. Stephens (2000), Warming of the world ocean, *Science*, *287*, 2225–2229, doi:10.1126/science.287.5461.2225.

Liu, L. L., W. Wang, and R. X. Huang (2008), The mechanical input to the ocean induced by tropical cyclones, *J. Phys. Oceanogr.*, *38*, 1253–1266.

Mann, M. E., and K. A. Emanuel (2006), Atlantic hurricane trends linked to climate change, *Eos Trans. AGU*, *87*(24), 233, doi:10.1029/2006EO240001.

Manning, D. M., and R. E. Hart (2007), Evolution of North Atlantic ERA40 tropical cyclone representation, *Geophys. Res. Lett.*, *34*, L05705, doi:10.1029/2006GL028266.

Maue, R. N., and R. E. Hart (2007), Comment on "Low frequency variability in globally integrated tropical cyclone power dissipation" by Ryan Sriver and Matthew Huber, *Geophys. Res. Lett.*, *34*, L11703, doi:10.1029/2006GL028283.

Pielke, R. A.Jr., and C. N. Landsea (1999), La Nina, El Nino, and Atlantic hurricane damages in the United States, *Bull. Am. Meteorol. Soc.*, *80*, 2027–2033, doi:10.1175/1520-0477(1999)080<2027:LNAENO>2.0.CO;2.

Price, J. F. (1981), Upper ocean response to a hurricane, *J. Phys. Oceanogr.*, *11*, 153–175, doi:10.1175/1520-0485(1981)011<0153:UORTAH>2.0.CO;2.

Santer, B. D., et al. (2006), Forced and unforced ocean temperature changes in Atlantic and Pacific tropical cyclogenesis regions, *Proc. Natl. Acad. Sci. U. S. A.*, *103*, 13,905–13,910, doi:10.1073/pnas.0602861103.

Scott, J. R., and J. Marotzke (2002), The location of diapycnal mixing and the meridional overturning circulation, *J. Phys. Oceanogr.*, *32*, 3578–3595, doi:10.1175/1520-0485(2002)032<3578:TLODMA>2.0.CO;2.

Shay, L. K., P. G. Black, A. J. Mariano, J. D. Hawkins, and R. L. Elsberry (1992), Upper ocean response to Hurricane Gilbert, *J. Geophys. Res.*, *97*, 20,227–20,248, doi:10.1029/92JC01586.

Shay, L. K., A. J. Mariano, S. D. Jacob, and E. H. Ryan (1998), Mean and near-inertial ocean current response to Hurricane Gilbert, *J. Phys. Oceanogr.*, *28*, 858–889, doi:10.1175/1520-0485(1998)028<0858:MANIOC>2.0.CO;2.

Shepherd, J. M., and T. Knutson (2006), The current debate on the linkage between global warming and hurricanes, *Geogr. Compass*, *1*, 1–24, doi:10.1111/j.1749-8198.2006.00002.x.

Sriver, R. L., and M. Huber (2006), Low frequency variability in globally integrated tropical cyclone power dissipation, *Geophys. Res. Lett.*, *33*, L11705, doi:10.1029/2006GL026167.

Sriver, R. L., and M. Huber (2007a), Reply to comment by R. N. Maue and R. E. Hart on "Low frequency variability in globally integrated tropical cyclone power dissipation", *Geophys. Res. Lett.*, *34*, L11704, doi:10.1029/2007GL029413.

Sriver, R. L., and M. Huber (2007b), Observational evidence for an ocean heat pump induced by tropical cyclones, *Nature*, *447*, 577–580, doi:10.1038/nature05785.

Trenberth, K. E., and J. Fasullo (2007), Water and energy budgets of hurricanes and implications for climate change, *J. Geophys. Res.*, *112*, D23107, doi:10.1029/2006JD008304.

Uppala, S. M., et al. (2005), The ERA-40 re-analysis, *Q. J. R. Meteorol. Soc.*, *131*, 2961–3012, doi:10.1256/qj.04.176.

Webster, P. J., et al. (2005), Changes in tropical cyclone number, duration, and intensity in a warming environment, *Science*, *309*, 1844–1846, doi:10.1126/science.1116448.

Wentz, F. J., C. Gentemann, D. Smith, and D. Chelton (2000), Satellite measurements of sea surface temperatures through clouds, *Science*, *288*, 847–850, doi:10.1126/science.288.5467.847.

Wentz, F. J., D. K. Smith, C. A. Mears, and C. L. Gentemann (2001), Advanced algorithms for QuikScat and SeaWinds/AMSR, paper presented at IGARSS'01, Inst. of Electr. and Electron. Eng., Sydney, N. S. W., Australia.

Wunsch, C., and R. Ferrari (2004), Vertical mixing, energy, and the general circulation of the oceans, *Annu. Rev. Fluid Mech.*, *36*, 281–314, doi:10.1146/annurev.fluid.36.050802.122121.

Zedler, S. E., et al. (2002), Analysis and simulations of the upper ocean's response to Hurricane Felix at the Bermuda Testbed Mooring site: 13–23 August 1995, *J. Geophys. Res.*, *107*(C12), 3232, doi:10.1029/2001JC000969.